Mechanical experimental characterisation and numerical modelling of an unfilled silicone rubber

Luc Meunier, Grégory Chagnon, Denis Favier, Laurent Orgéas, Pierre Vacher

Mechanical experimental characterisation and numerical modelling of an unfilled silicone rubber

L. Meunier[a], G. Chagnon[a,*], D. Favier[a], L. Orgéas[a], P. Vacher[b]

[a]Université de Grenoble/CNRS, Laboratoire 3S-R, Cedex 9, 38041 Grenoble, France
[b]Université de Savoie, Laboratoire SYMME, Polytech Savoie, Domaine Universitaire BP 80439, 74944 Annecy le Vieux, France

In this paper, the mechanical behaviour of an unfilled silicone rubber is analysed. Firstly, silicone samples were subjected to five homogeneous tests: tensile, pure shear, compression, plane strain compression and bulge tests. During the tests, full-field measurements of the strain on the surface of deformed samples were obtained using a Digital Image Correlation technique. Results show that the Mullins effects and hysteresis, as well as strain rate sensitivity, can be considered as negligible. Results also emphasise the influence of the loading path. Then, five well-known hyperelastic models (neo-hookean, Mooney, Gent, Haines and Wilson and Ogden models) were fitted to the experimental data. Finally, a heterogeneous test was realised by stretching a silicone plate sample containing holes. Finite element simulations of this experiment have been performed with the hyperelastic models. The comparison of experimental and numerical results emphasises the importance of the choice of the hyperelastic modelling in the simulation of strain fields.

1. Introduction

Owing to their good bio-compatibility, silicone rubbers are being increasingly used in bio-medical applications. Unfortunately, experimental studies aimed at analysing and modelling the mechanical behaviour of such materials are quite scarce and limited to filled materials. For example, the article in Ref. [1] presents a uniaxial loading–unloading test performed on electro-active silicone rubbers. Results illustrate a non-linear reversible behaviour with weak hysteresis. More comprehensive experimental studies are described in Refs. [2,3] on a silica filled silicone. Authors highlight the Mullins effect [4] and cyclic relaxation during cyclic tensile tests. In order to improve the modelling of bio-implants, the study in Ref. [5] used pure shear, uniaxial and biaxial tests to evaluate the behaviour of another filled silicone rubber. This material presented a large Mullins effect. Furthermore, tensile and compression tests performed

on a filled silicone rubber are presented in Ref. [6]. This article emphasises the strain rate dependency of silicone behaviour. A wide range of strain rates were tested during a compression test from 10^{-3} to $10^3 \, \text{s}^{-1}$ showing a strain rate dependency only when strain rate exceeds $40 \, \text{s}^{-1}$: multiplying the strain rate by 100 can multiply stress levels by 4 in this domain.

Thus, only a few articles develop experimental studies and comparative modelling of filled silicone rubbers and none of them study unfilled silicone rubber. Hence, there is a lack of information for the development of structural applications involving silicone rubber parts. Within that context, the purposes of this article are (i) to characterise and understand the mechanical behaviour of an unfilled silicone rubber under various mechanical loading, (ii) to fit its behaviour with commonly used constitutive models and (iii) to assess the capability of these models to represent the behaviour of the silicone not only under homogeneous, but also under heterogeneous, loading conditions. Hence, material preparation procedures are described in Section 2. Details of specimens as well as testing apparatus

* Corresponding author. Tel.: +33 476827085; fax: +33 476827043.
  E-mail address: gregory.chagnon@hmg.inpg.fr (G. Chagnon).

which have been used for simple tensile, pure shear, bulge, simple compression and plane strain compression tests are described in Section 3. Section 4 presents experimental results. In particular, the lack of different irreversible phenomena is underlined. This permits modelling of the mechanical behaviour of the studied silicone within the scope of hyperelasticity as presented in Section 5. Five well-known hyperelastic models are chosen to fit experimental data: neo-hookean [7], Mooney [8], Ogden [9], Haines and Wilson [10] and Gent [11] models. Lastly, in order to test the ability of the above constitutive schemes to model the deformation of complex structures, a silicone plate containing holes is deformed in tension (Section 6). Finite element simulations of this experiment are performed with the fitted hyperelastic models, and a comparison of experimental and numerical local strain fields is achieved.

2. Materials – preparation procedures

The chosen silicone rubber is an unfilled formulation produced by Rhodia (RTV 141). Specimens were produced using the following processing route: (i) mixing the two liquid components, i.e., the uncured silicone and the curing agent, with a 10/1 ratio, (ii) putting the uncured mixture under vacuum for 30 min in order to eliminate undesirable entrapped bubbles, (iii) injecting the liquid mixture in moulds with a medical syringe, (iv) putting moulds inside an oven at 70 °C for 150 min to cure the silicone. Thereafter, some of the external surfaces of the moulded samples were coated with a random pattern made of small speckles in order to allow digital image correlation (DIC) for the measurement of the local strain field (see next Section). Note that the quality of the coated pattern is critical to gain a good estimation of the strain field.

Different procedures were used to obtain the desired test piece geometries. Compression, plane strain compression and bulge specimens were directly moulded in specially designed moulds. Tensile, pure shear and plate with holes were cut from large sheets using hollow punches. Particular attention was paid during preparation in order to obtain specimens with reproducible mechanical properties.

3. Mechanical testing procedure

3.1. Strain field measurements

During the tensile, pure shear, bulge and heterogeneous tests, the deformation of samples and their superimposed speckles pattern were recorded using a CCD camera. Using the Digital Image Correlation Software 7D [12,13], it was then possible to determine the local strain field on the surface of the deformed samples. The DIC technique already used to characterise rubbers (see for example Ref. [14]) also permits demonstrating the homogeneity of the strain field during "homogeneous" tests. Tensile and pure shear tests pictures were recorded with a JAI CCD camera (1280×1024 pixels, 25 Hz, (see Fig. 1)). In the case of the plate with holes, a different camera with a 10 megapixel sensor (3872×2592 pixels) was used to improve the resolution of the images, so that the estimation of the local
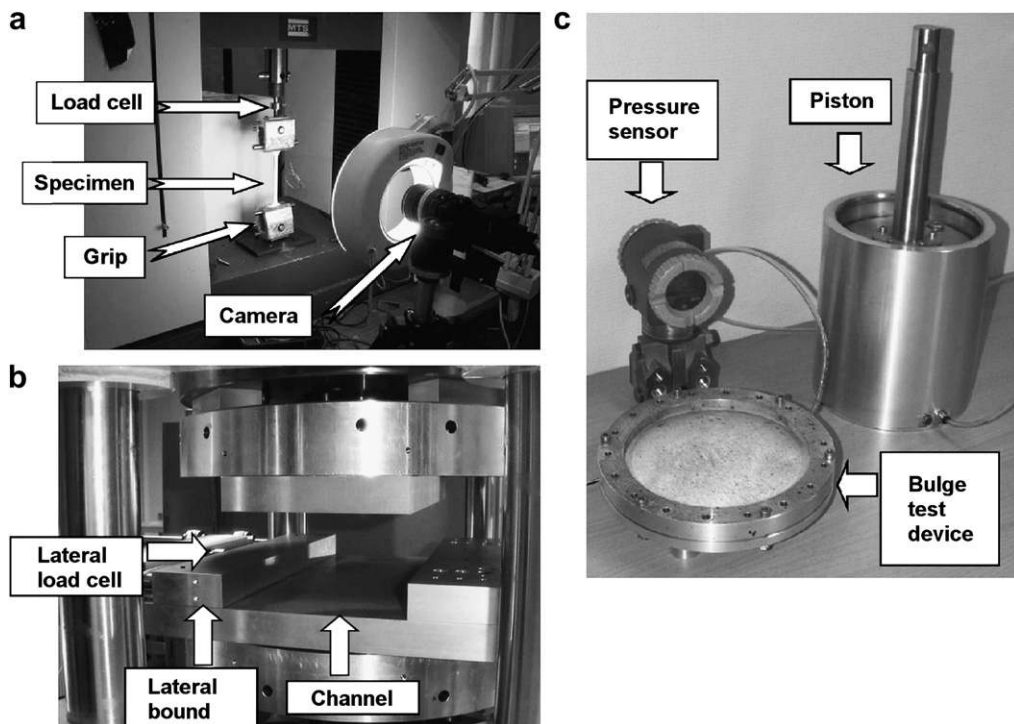

Fig. 1. Experimental devices (a) testing machine with tensile test specimen and CCD camera, (b) rheometer used for compression tests, (c) inflating device with pressure sensor and piston.

strain field was more accurate. For the bulge test, 3D measurements were needed, therefore two identical commercial CCD cameras were used (3872 × 2592 pixels). The obtained pictures were also processed by 7D software. This is also able to perform 3D stereo-correlation which gave: (i) the local strain field of samples and (ii) the geometry of the surface of the deformed sample as well as the displacements. As an example, Fig. 2 shows a 3D image reconstructed by 7D during a bulge test performed at a bulge pressure of 150 mbar.

3.2. Investigated mechanical loadings

All the tested samples were deformed using a universal mechanical testing machine (MTS 4M). In order to analyse the mechanical behaviour of the silicone, samples were subjected to five different homogeneous loadings and one heterogeneous. Note that in order to analyse tests the silicone was assumed to be incompressible.

- Simple tensile tests were performed on dumbbell shaped samples having an initial gauge length l_0 of 60 mm, a gauge width $b_0 = 12$ mm and a gauge thickness $e_0 = 2$ mm. The specimen was held in self-tightening grips as presented in Fig. 3(a), with the upper one connected to a load cell (Entran ELPM 250 N). During the test, the nominal stress tensor (First Piola–Kirchhoff stress tensor) $\Pi = \Pi_{xx}\overrightarrow{e}_x \otimes \overrightarrow{e}_x$ is assumed to be homogeneous within the gauge region as well as the deformation gradient tensor:

$$F = \lambda_{xx}\overrightarrow{e}_x \otimes \overrightarrow{e}_x + \left(\overrightarrow{e}_y \otimes \overrightarrow{e}_y + \overrightarrow{e}_z \otimes \overrightarrow{e}_z\right)/\sqrt{\lambda_{xx}}$$

The axial stress $\Pi_{xx} = f_x/(b_0 e_0)$ and the axial elongation $\lambda_{xx} = l/l_0$ were obtained from the measurements of axial force f_x and DIC results, respectively.

- Pure shear strain state was approached by performing plane strain tensile tests (see Fig. 3(b)). The initial height l_0, the constant width b_0 and the thickness e_0 of samples were 6 mm, 70 mm and 2 mm, respectively. The same equipment as for the tensile test was used. As in the previous test, the load cell gives the axial force f_x which leads to estimate the component $\Pi_{xx} = f_x/(b_0 e_0)$ of the stress tensor:

$$\Pi = \Pi_{xx}\overrightarrow{e}_x \otimes \overrightarrow{e}_x + \Pi_{yy}\overrightarrow{e}_y \otimes \overrightarrow{e}_y$$

Also, the strain state during the test was supposed to be homogeneous and the deformation gradient tensor was expressed as:

$$F = \lambda_{xx}\overrightarrow{e}_x \otimes \overrightarrow{e}_x + \overrightarrow{e}_y \otimes \overrightarrow{e}_y + 1/\lambda_{xx}\overrightarrow{e}_z \otimes \overrightarrow{e}_z$$

Once again, $\lambda_{xx} = l/l_0$ is obtained from DIC.

- A simple compression test was made on a cylindrical specimen with initial diameter D_0 and height h_0 equal to 37 mm and 20 mm, respectively (see Fig. 3(c)). Tests were carried out using a rheometer which was originally developed to analyse the rheology of concentrated fibre suspensions [15]. The compression platens were coated with silicone grease in order to limit friction between them and the samples. The sample height h is measured by the machine and allows the calculation of the degree of compression $\lambda_{xx} = h/h_0$. Symmetry and incompressibility lead to the deformation gradient tensor:

$$F = \lambda_{xx}\overrightarrow{e}_x \otimes \overrightarrow{e}_x + \left(\overrightarrow{e}_y \otimes \overrightarrow{e}_y + \overrightarrow{e}_z \otimes \overrightarrow{e}_z\right)/\sqrt{\lambda_{xx}}$$

The stress state is $\Pi = \Pi_{xx}\overrightarrow{e}_x \otimes \overrightarrow{e}_x$ where $\Pi_{xx} = 4f_x/(\pi D_0^2)$ is known from the measurement of the compression force f_x, here measured with a 5000 N load cell.

- A planar compression test was conducted on rectangular blocks. The initial length l_0, width b_0 and height h_0
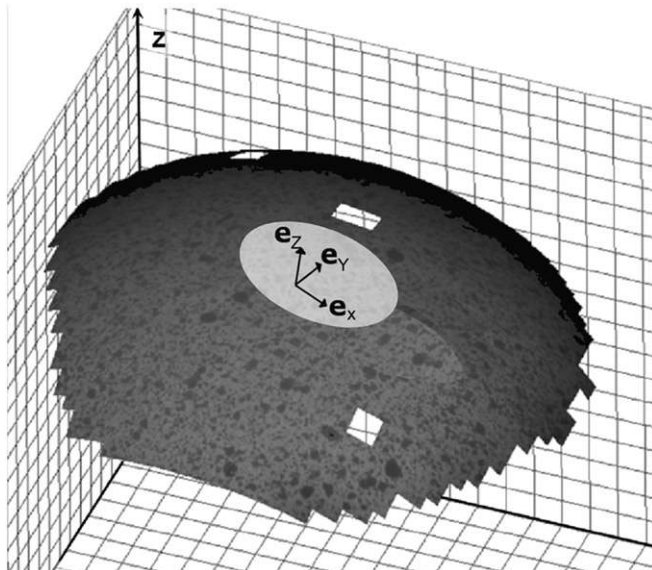

Fig. 2. DIC reconstruction of the 3D deformed surface of a silicone disk subjected to a bulge test at $P = 150$ mbar.
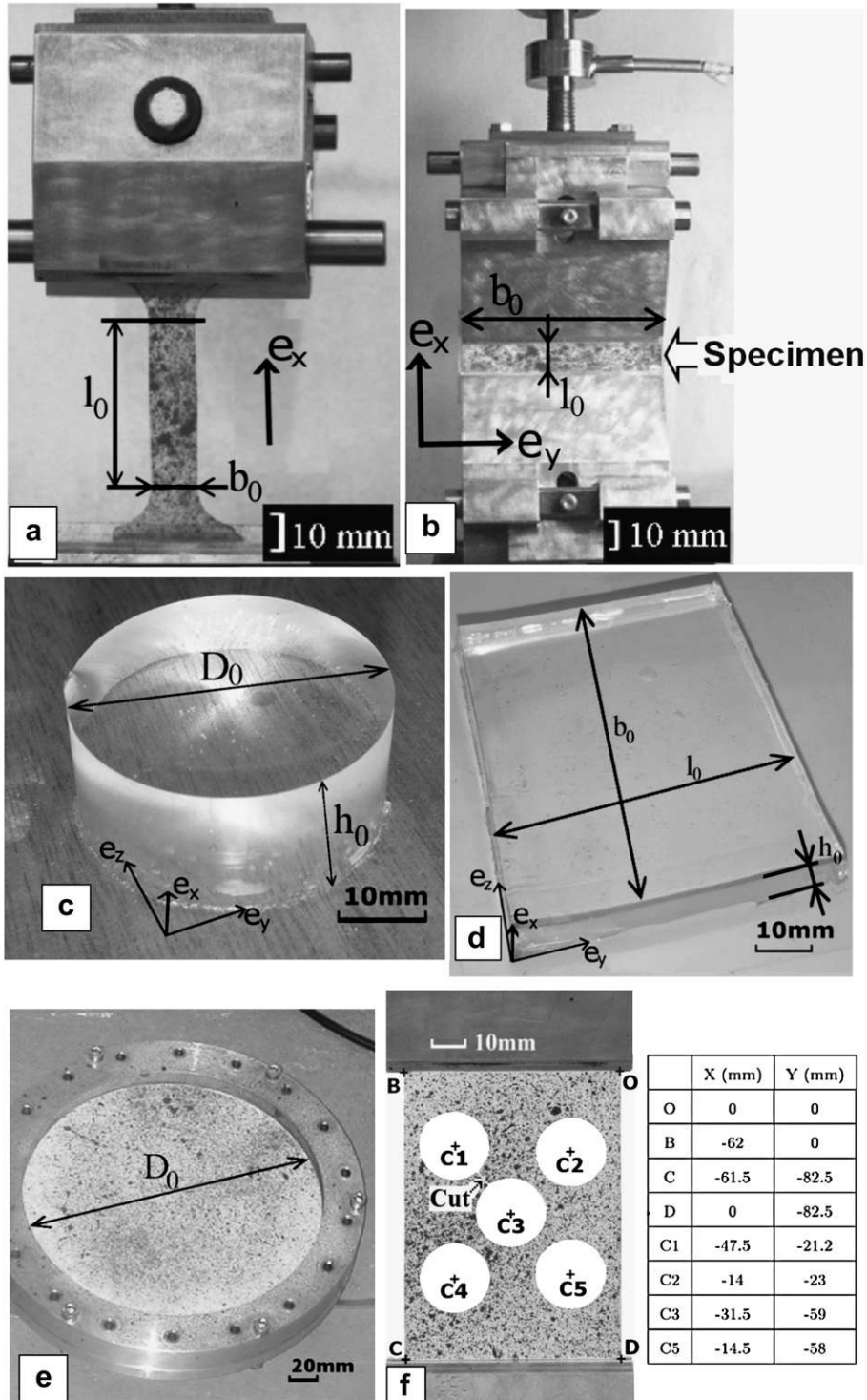
Fig. 3. Specimens used for: (a) tensile tests, (b) pure shear, (c) simple compression tests, (d) plane strain compression tests, (e) bulge tests, (f) heterogeneous tests and specimen dimensions.

of the blocks were 60 mm and 11 mm, respectively (see Fig. 3(d)). Tests were performed in the same rheometer for the compression tests but the platens were modified to ensure a planar strain state as illustrated in

Fig. 1(b). Furthermore, one of the lateral restraints was connected to a load cell (Entran 2500 N) so as to measure the lateral force f_z. The sample width b_0 was kept constant during the test by preventing the normal

displacement on two opposite sides of the channel (see Fig. 1(b)). Thus, the deformation gradient tensor is:

$$F = \lambda_{xx}\overrightarrow{e}_x\otimes\overrightarrow{e}_x + 1/\lambda_{xx}\overrightarrow{e}_y\otimes\overrightarrow{e}_y + \overrightarrow{e}_z\otimes\overrightarrow{e}_z$$

where $\lambda_{xx} = h/h_0$. In this case, the stress tensor is:

$$\Pi = \Pi_{xx}\overrightarrow{e}_x\otimes\overrightarrow{e}_x + \Pi_{zz}\overrightarrow{e}_z\otimes\overrightarrow{e}_z$$

where $\Pi_{xx} = f_x/(b_0h_0)$ and the axial force f_x as well as the lateral force f_z were measured by load cells [15].

- A bulge test was also conducted. Tested specimens were disks of initial diameter $D_0 = 200$ mm and thickness $e_0 = 2$ mm. An undeformed specimen which is held in the bulge test machine can be seen in Fig. 3(e). The bulge test machine is an independent inflating device shown in Fig. 1(c). This equipment consists of a piston connected to a device that holds the specimen. The piston is driven by the MTS testing machine to inflate the specimen with air. The pressure is measured with a pressure sensor (Foxboro 0–500 mbar). Due to the symmetry of the machine, the mechanical loading and the assumed isotropy of the material, the curvature of the inflated sample was presumed to be the same along all directions at the disk centre. The deformation gradient tensor in a local coordinate system ($\overrightarrow{e}_x, \overrightarrow{e}_y, \overrightarrow{e}_z$, see Fig. 2) is:

$$F = \lambda_{xx}(\overrightarrow{e}_x\otimes\overrightarrow{e}_x + \overrightarrow{e}_y\otimes\overrightarrow{e}_y) + 1/\lambda_{xx}^2\overrightarrow{e}_z\otimes\overrightarrow{e}_z$$

where λ_{xx} is the elongation in the tangential direction of the specimen and is measured by DIC. As $D_0 \gg e_0$, the stress is also assumed to be constant along the thickness. With these hypotheses, the stress tensor is:

$$\Pi = \Pi_{xx}(\overrightarrow{e}_x\otimes\overrightarrow{e}_x + \overrightarrow{e}_y\otimes\overrightarrow{e}_y) + \Pi_{zz}\overrightarrow{e}_z\otimes\overrightarrow{e}_z$$

where the component Π_{xx} can be calculated from knowledge of both the curvature radius R and the tangential elongation λ_{xx} measured during the test from DIC. Indeed, $\Pi_{xx} = PR\lambda_{xx}/(2e_0)$ where P is the pressure which is recorded during the test.

- A tensile test was also performed on a sheet (initial height $l_0 = 80$ mm, width $b_0 = 60$ mm, thickness $e_0 = 1.75$ mm) containing five holes of diameter 20 mm, as shown in Fig. 3(f). The position of the centres of the holes and the corners are given in the table of Fig. 3. A cut was made between the upper left and the centre holes as shown in Fig. 3. The test was conducted using the same equipment (grips, load cell) as for tensile and pure shear tests. The axial load cell measured the global force f_x and the DIC gave the in-plane strain field.

4. Homogeneous tests

4.1. Cyclic behaviour

A first cyclic tensile test was achieved in order to detect possible Mullins effect or hysteresis. For that purpose, load/unload sequences were made at six increasing stress levels with an elongation rate $\dot{\lambda}_{xx} = \dot{l}/l_0 = 8\times 10^{-3}$ s^{-1}. Results

have been sketched in the graph in Fig. 4. Stress–elongation curves show a perfect non-linear and reversible behaviour with no Mullins effect nor hysteretic loop: all loading and unloading curves are superimposed.

4.2. Influence of the rate of deformation

The influence of the rate of deformation on the behaviour of the silicone has been first studied by subjecting a tensile specimen to a load/unload sequence at different elongation rates $|\dot{\lambda}_{xx}| = 2\times 10^{-4}$ s^{-1} and 10^{-1} s^{-1}. Corresponding axial stress–elongation curves have been plotted in Fig. 5: there is no noticeable difference between the two cycles so that the silicone behaviour can be assumed independent of the rate of deformation, at least within the considered strain rate range.

In order to reinforce the last observation, a relaxation tensile test was performed. After stretching a tensile specimen at $\lambda_x = 2$ the elongation was kept constant and the global force f_x was measured for 2 h. As shown in Fig. 6, the nominal stress Π_{xx} diminished by less than 2% during such a relaxation sequence. Consequently, it is concluded from the results gained in these two subsections that the RTV 141 exhibits a non-linear elastic behaviour with very little time and rate of deformation dependency and without Mullins effect and hysteresis.

4.3. Influence of the mechanical loading

In the graphs of Fig. 7, the evolution of the first principal stress is reported (Π_{xx} for tensile, pure shear and compression and bulge tests) as a function of the principal elongation (λ_{xx} for tensile, pure shear and compression and bulge tests), for the five investigated homogeneous tests. For the two compression tests, the axial stress exhibits a monotonic strain hardening with constant curvature. Such a strain hardening is stiffer during plane strain compression. For the other loadings, the strain hardening is also emphasised,
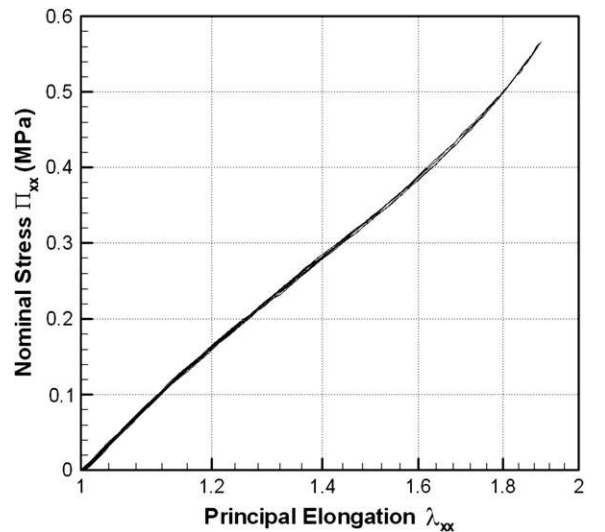

Fig. 4. Cyclic loading–unloading tensile test with increasing maximum stress: 0.1, 0.14, 0.2, 0.28, 0.4, 0.56 MPa.
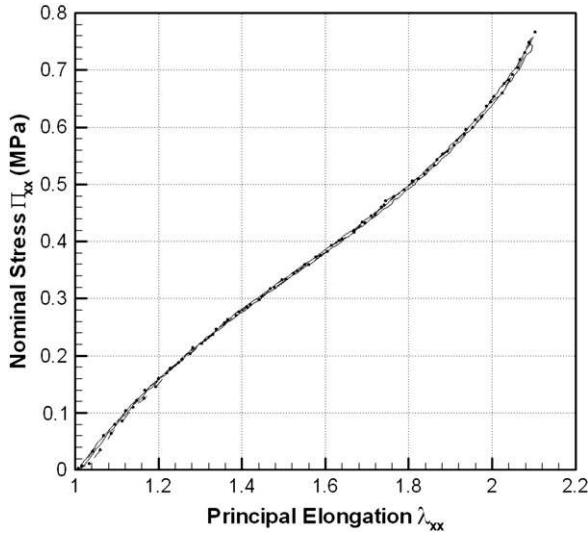
Fig. 5. Tensile test: two load/unload cycles performed at two elongation rates: (—) $2 \cdot 10^{-4} \, s^{-1}$ and (- ·) $10^{-1} \, s^{-1}$.
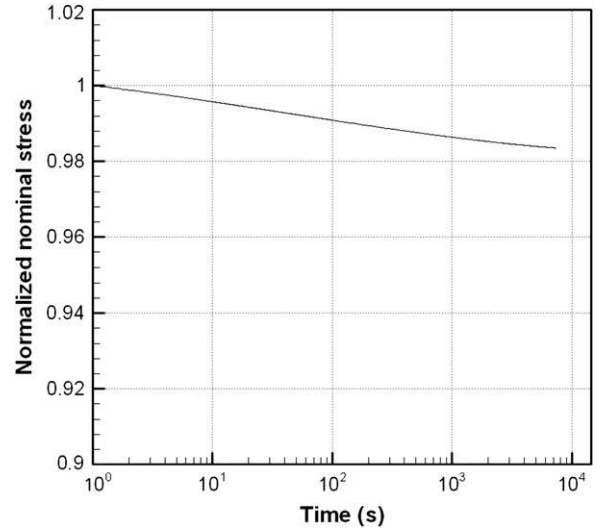

Fig. 6. Time evolution of the normalised stress $\Pi_{xx}/\Pi_{xx}(t = t_0)$, for a stress relaxation test recorded after a monotonic tensile test performed at $\lambda = 2$.

but systematically exhibits an inflection point, similar to that observed in many other elastomers. As for the compression loadings, stress levels recorded for the plane strain tension (pure shear) test are higher than those obtained in simple tension, but lower than those recorded during the bulge test.

These results highlight the strong influence of the type of mechanical loading on stress–elongation curves.

5. Discussion and constitutive modelling

It has been shown in the previous part that the material's behaviour does not present irreversible effects and does not depend on its history; it only depends on its current strain state. Thus, it has a non-linear elastic behaviour that could be represented by hyperelastic constitutive

equations. This kind of modelling describes the strain energy density W of the material, which is the elastic energy stored by the material during the loading.

5.1. Elastic energies during homogeneous tests

Using the experimental data, strain energy densities per unit volume could be calculated for the five homogeneous tests through the equation:

$$W = \int_F \Pi : dF$$

Most hyperelastic constitutive equations for isotropic material are written as functions of the two first invariants I_1 and I_2 of the dilatation tensor $C = F^T F$, with $I_1 = Tr(C)$ and
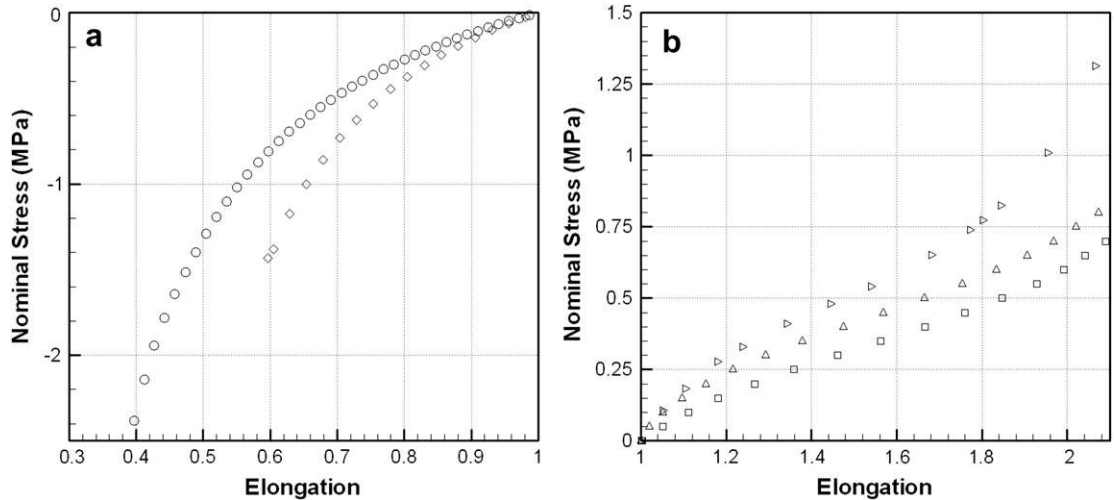

Fig. 7. Principal stress–elongation curves obtained in: (a) (○) simple compression, (◇) plane strain compression; (b) (□) uniaxial tensile, (△) pure shear and (▷) bulge tests.

$I_2 = 0.5 \times [I_1^2 - Tr(C^2)]$. This is the case of the Rivlin series [16], Haines and Wilson [10], neo-hookean [7], Mooney [8], etc. In this way, the energy density of each test has been sketched in Fig. 8 as function of I_1 and I_2 to give indications for the choice of a constitutive equation. In a first approach, the different strain energies evaluated for each test can be considered as a function of the first strain invariant. It even seems linear according to the first invariant. This corresponds to the neo-hookean model [17] $W = C_1(I_1 - 3)$ with $C_1 = 0.175$ MPa. Fig. 9 presents a comparison between model simulations and experimental data. Compression tests are relatively well depicted by this model (see Fig. 9(a)) but it cannot predict tensile, pure shear and bulge tests when the elongation exceeds 1.6 (see Fig. 9(b)). It also predicts too high stress levels for the tensile test and too low stress levels for bulge test. Moreover, this kind of constitutive equation cannot represent the strain hardening, as can be seen in Fig. 9(b) for high elongations. Nevertheless, it is efficient for a only one parameter model. To have more precise predictions of the material's behaviour, more complex constitutive equations are needed.

5.2. Hyperelastic energy density parameter fit

Four hyperelastic constitutive equations have been chosen: Mooney [8], Haines and Wilson [10], Gent [11] and Ogden [9]. The first three depend on the invariants of the right Cauchy–Green tensor C, whereas the last one is written in terms of principal elongations. Hyperelastic constitutive equations are presented in Table 1. These models have been chosen because they are representative, but not exhaustive, of widely used hyperelastic constitutive equations. The Mooney model is the most used in rubber industrial development because of its simplicity and its good representation of moderate deformations. Haines and Wilson is a high order Rivlin series [16], whereas the Gent model represents the non-Gaussian hyperelastic laws [17] due to its equivalence with the eight-chain model

[18]. Moreover, it is equivalent to the Hart–Smith [19] model [20]. Lastly, the Ogden model has been chosen for its high versatility which allows it to fit almost any experimental data. Mooney and Gent models have only two parameters whereas Haines and Wilson, and Ogden models (in its classical form) use six parameters.

The strain energy density parameters have been fitted on experimental data from tensile, pure shear, compression, plane strain compression and bulge tests. The optimization process used a conjugate gradient algorithm of Scilab software to minimise the error $\text{Error}_{\text{model}}$ with respect to the model's parameters. The error of a constitutive equation was defined as follows for each kind of homogeneous loading:

$$\text{Error}_{\text{loading}} = \frac{1}{N} \sum_{j=1}^{N} \left[\Pi_{\text{exp}}(\lambda_j) - \Pi_{\text{sim}}(\lambda_j) \right]^2$$

where N is the number of experimental points, λ_j the elongations of the experimental data, $\Pi_{\text{exp}}(\lambda_j)$ is the experimental stress and $\Pi_{\text{sim}}(\lambda_j)$ is the simulated stress for the evaluated model. The global error of a model $\text{Error}_{\text{model}}$ was then defined as the mean of the five $\text{Error}_{\text{loading}}$ figures. The values of the fitted parameters are presented in Table 2. Fig. 10 presents a comparison between experimental data for the homogeneous loadings and the predictions of the four fitted models. Compression and plane strain compression tests data (Fig. 10(c) and (d)) are well depicted by all constitutive equations, but this is not so for the other three tests. Indeed, results given here show that the Mooney model can only describe the silicone rubber at low strains because it is unable to represent the strain hardening of the material. On the contrary, Gent, Ogden and Haines and Wilson models have good predictions for the whole curves. However, the Gent model seems less accurate: the curves show a difference with experimental slope at high elongations in bulge, tensile and shear tests. The considered silicone presents a weak strain hardening because it is unfilled; as a consequence the Gent model is not the
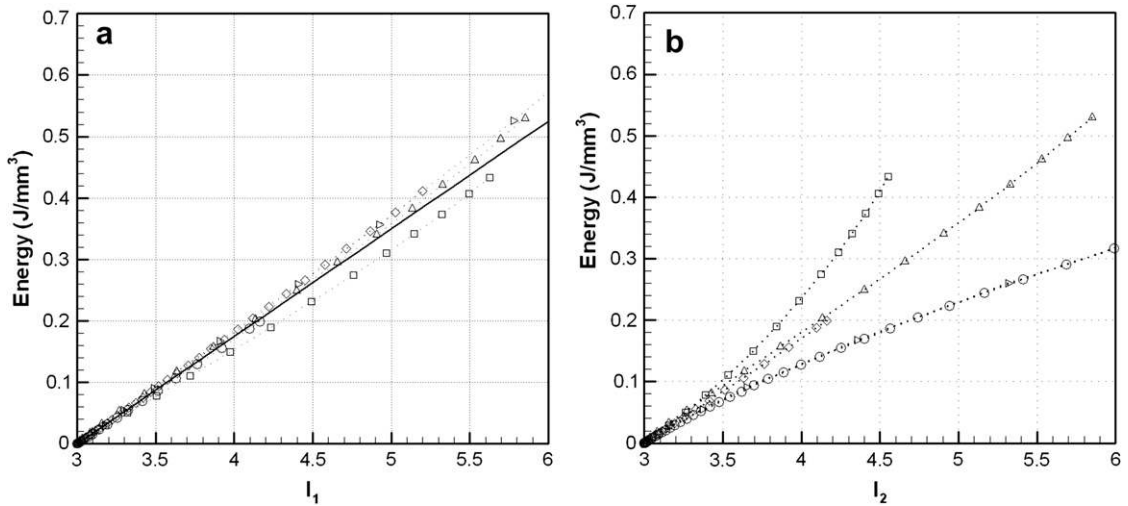

Fig. 8. Evolution of the elastic energy density as a function of (a) I_1 and (b) I_2 for the five homogeneous tests performed for fit: ($\square$) uniaxial tensile, ($\triangle$) pure shear, ($\circ$) simple compression, ($\diamond$) plane strain compression and ($\triangleright$) bulge test. The fitted neo-hookean model is also represented (—).
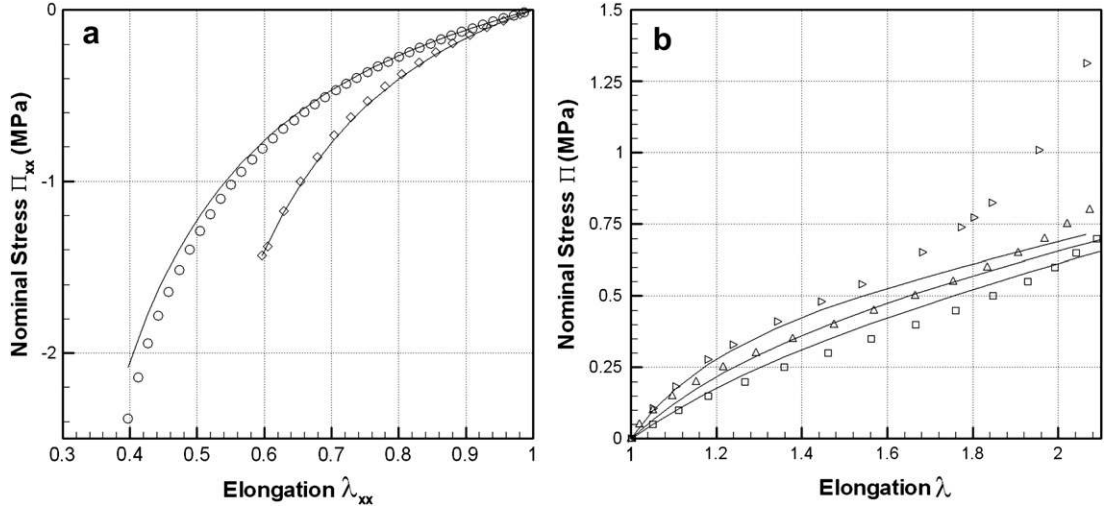
Fig. 9. Nominal stress measured and predicted by the neo-hookean model for the five tests: (□) uniaxial tensile, (△) pure shear, (○) simple compression, (◇) plane strain compression and (▷) bulge test for (a) compression tests and (b) traction tests.

best adapted model since it presents a strong strain hardening.

Fig. 11 presents the lateral stress measured during the plane strain compression test. These data were not used to fit the models but are given to make a comparison of the predictions of the constitutive equations. Note that the experimental curve indicates a horizontal tangent at the origin. This can be explained by the layer of grease and by a possible clearance between the lateral restraint and the specimen. The curves indicate that Mooney, Haines and Wilson and Ogden give about the same results, while only Gent provides a better approximation of the experimental data. Thus, there are still some limits to the modelling for this silicone rubber at large elongations since the lateral stress could not be well depicted. It can also be noted that experimental and model slopes at high elongation for the bulge test are very different. In that case, the silicone is much stiffer than the prediction of any of the models. This could also be due to the fact that these points are at the limit of the fit domain.

In conclusion, except for the Mooney constitutive equation, the models seem adequate to represent this silicone rubber. Nevertheless, Haines and Wilson and Ogden model parameters are more difficult to fit because of the number of parameters, whereas Gent needs only two parameters with a physical meaning. Note that the Haines and Wilson constitutive equation requires six parameters that allow it to fit to almost any hyperelastic experimental curve but it can also introduce numerical problems during calculation [21].

6. Heterogeneous test

To evaluate the ability of the models to describe a complete structure, a specimen generating heterogeneous strain fields has been used (as described in Section 3.2).

6.1. Experimental results

The specimen has been submitted to a force of 20 N and the strain field was measured. Fig. 12 shows the photography used for DIC and the associated representation of the major principal elongation field at a force of 20 N. Some voids are visible in Fig. 12(b) owing to local correlation problems related to too large speckles in the pattern. The elongation field shows great heterogeneity: most of the plate has an in-plane maximal elongation lower than 1.5, whereas the most stretched parts have a maximal elongation higher than 2.5: the areas between the exterior edges and the holes or between two holes are very stretched due to section reduction in these areas. Furthermore, the cut induced even higher elongations.

6.2. Numerical model

The numerical simulations of the above experiments were performed with the finite element code ABAQUS, the model parameters are those given in Table 2. The Gent model required the development of a UHYPER subroutine, while Mooney, Haines and Wilson and Ogden

Table 1
Hyperelastic energy density constitutive equations

Mooney	$W_M = C_{10}(I_1 - 3) + (I_2 - 3)$
Gent	$W_G = -\frac{E}{6}J_m \ln[1 - \frac{I_1 - 3}{J_m}]$
Haines and Wilson	$W_{HW} = \frac{C_{10}(I_3 - 3) + C_{20}(I_1 - 3)^2 + C_{30}(I_1 - 3)^3}{C_{01}(I_2 - 3) + C_{20}(I_2 - 3)^2 + C_{11}(I_2 - 3)(I_1 - 3)}$
Ogden	$W_O = \sum_{i=1}^{n} \frac{\mu_i}{\alpha_i}(\lambda_1^{\alpha_i} + \lambda_2^{\alpha_i} + \lambda_3^{\alpha_i} - 3)$

Table 2
Values of the hyperelastic energy parameters fitted on experimental data from all homogeneous tests

Mooney	$C_{10} = 0.14$	$C_{01} = 0.023$	
Gent	$E = 0.97$	$J_m = 13$	
Haines and Wilson	$C_{10} = 0.14$	$C_{20} = -0.0026$	$C_{10} = 0.0038$
	$C_{01} = 0.033$	$C_{02} = 0.00095$	$C_{11} = -0.0049$
Ogden	$\mu_1 = 0.46$	$\mu_2 = 0.00027$	$\mu_1 = -0.0074$
	$\alpha_1 = 1.4$	$\alpha_2 = 10$	$\alpha_3 = -3.3$

8

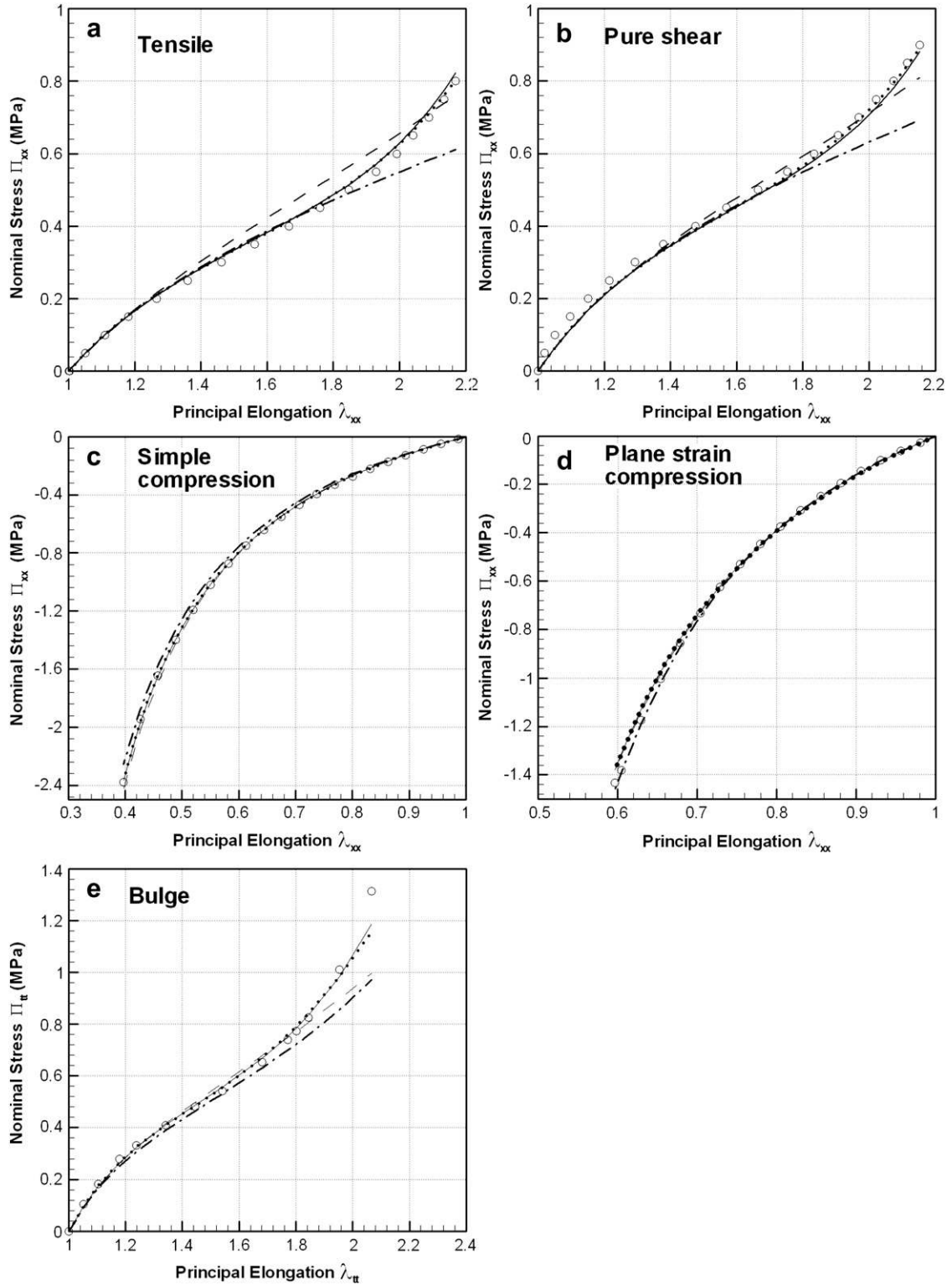**Fig. 10.** Experimental data (○) and simulations of the four hyperelastic constitutive equations, (·−·) Mooney, (- -) Gent, (···) Haines and Wilson and (—) Ogden for (a) tensile, (b) pure shear, (c) compression, (d) plane strain compression and (e) bulge test. The principal elongation used for the horizontal axis is in the loading direction (a,b,c,d) and in a tangential direction of the plate (e).
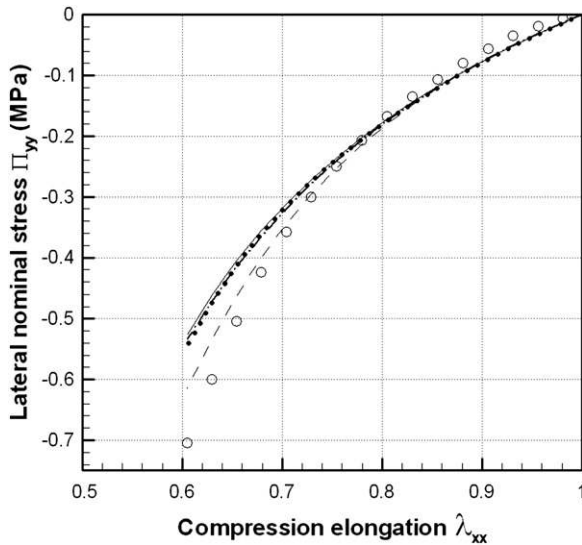
Fig. 11. Experimental data (○) and model predictions ((·−·) Mooney, (- -) Gent, (···) Haines and Wilson and (—) Ogden) for the lateral stress during the plane strain compression test.

models were already implemented in ABAQUS. The material models were defined as incompressible: quadratic (CPS8) elements were used, the corresponding mesh is presented in Fig. 13. The finite element model geometry was designed using the dimensions given in the table of Fig. 3. A 2D plane stress model was designed since (i) the thickness is fairly homogeneous (1.75 mm ± 0.02 mm) (ii) the lateral surfaces of the plates are free of load. The lower side of the model is fixed and the upper face is subjected to

(i) rigid body vertical displacement and (ii) the global force f_x is applied on this face.

6.3. Comparison at imposed load

The simulations are performed with an imposed load f_x of 20 N. Fig. 14 shows a comparison between the photograph of the deformed specimen and the shape predicted by the simulations (black outlines). As evident from this figure, the model simulations involving the Mooney model greatly overestimates the deformed shape of the specimen, while predictions given by the Gent model are much better, but slightly stiffer than experiment, and those given by Haines and Wilson and Ogden models are fairly good. These results confirm what could be seen on tensile curves: the Mooney model cannot represent the strain hardening (see Fig. 10(a)), even moderate, of this material, hence it predicts too large displacements for the imposed load. The Gent model does not fully represent the material for all the homogeneous tests, especially the tensile test. It predicts too high a stiffness at moderate strain (for elongation between 1.4 and 2 in Fig. 10(a)), which could explain the smaller displacements predicted by the simulation.

The comparison of the shapes made above only gives a global point of view, therefore, another comparison tool has been used: the maximal elongation along a path was studied to compare the local simulated elongation to the experimental elongation. The chosen path passes through the upper holes, as shown in Fig. 13, in order to study the most stretched parts of the plate. The curves describing the experimental and simulated major elongation along the path are presented
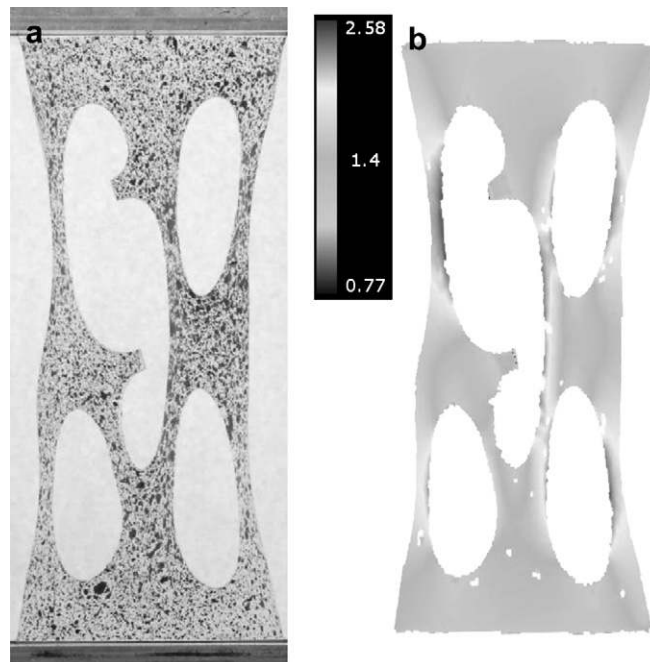

Fig. 12. Photograph of the deformed plate for an applied force of 20 N: (a) deformation of the pattern, (b) colour map: major principal elongation (result of 7D).
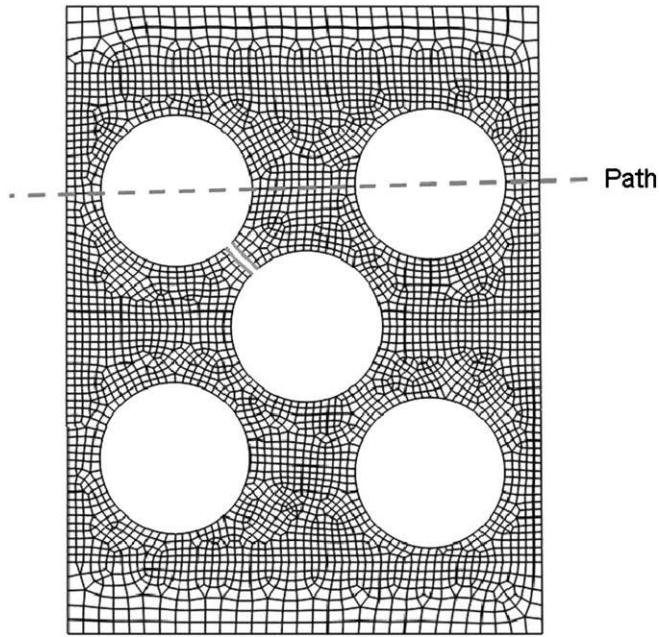
Fig. 13. FE mesh and path from which the strain data are extracted.

in Fig. 15 for a loading of 20 N. Predictions of the Mooney model are good only for moderate deformation. Indeed, the Mooney predictions become too soft for large deformations, thus introducing important errors (60% of elongation on the right side of the path). Conversely, predictions given by Gent, Ogden and Haines and Wilson models still fit to the experimental data well even for large elongations.

6.4. Comparison at imposed displacement

Another comparison was made here: it was shown that the Mooney constitutive equation cannot represent the experiment at the imposed load but how its capacity to predict the displacements and the strain fields when using an imposed displacement of boundaries was considered. Thereby, the imposed displacement on the upper side of
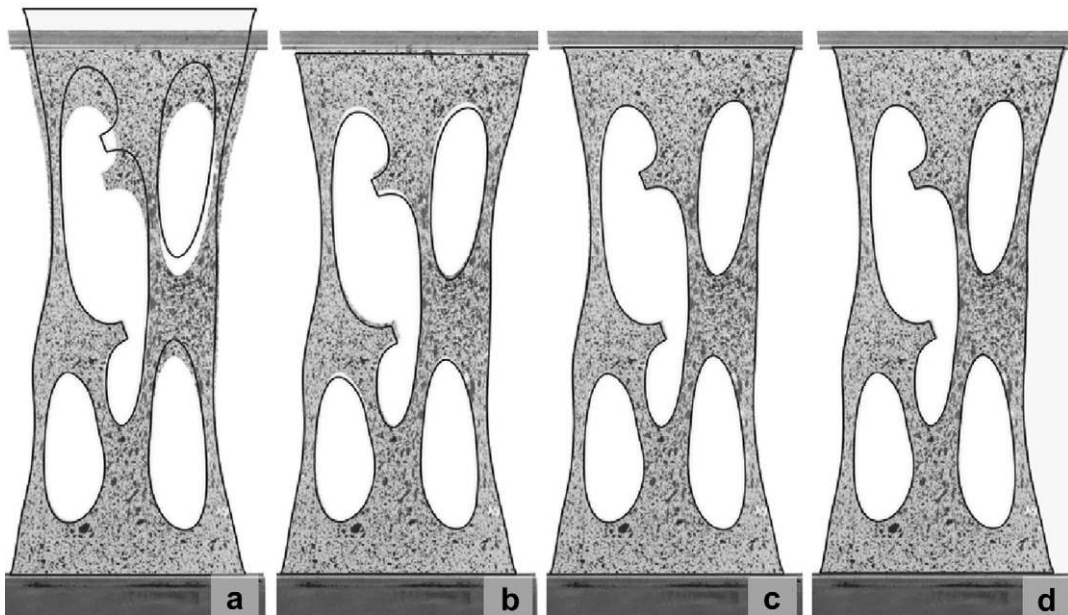

Fig. 14. Photograph and shape predicted by simulation of the plate with holes submitted to 20 N for the models: (a) Mooney, (b) Gent, (c) Haines and Wilson and (d) Ogden.
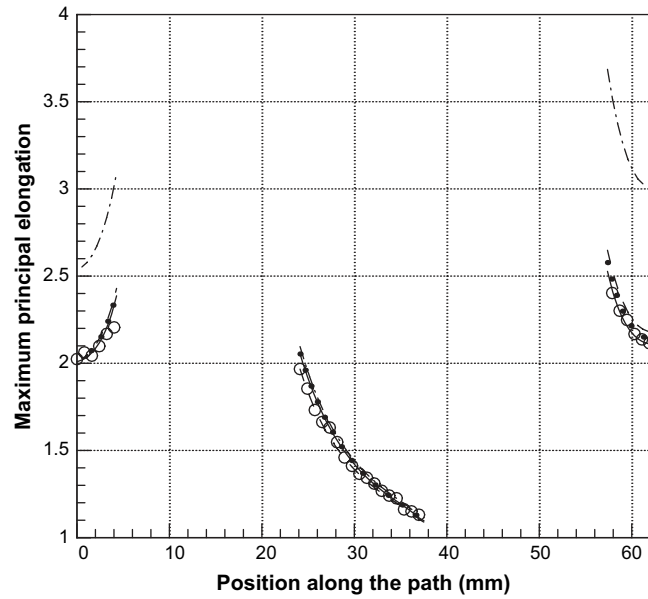
Fig. 15. Experimental and simulated elongations along the path defined in Fig. 14 at 20 N: (○) experimental data, (·–·) Mooney, (- -) Gent, (···) Haines and Wilson and (—) Ogden; the blank in the curves are due to the holes.

the model is 57.3 mm, which is the experimental displacement of the upper side of the plate at 20 N. As the other three models already gave results in good agreement with the experiment, they are not presented in this part. The shape of the model is superimposed on the photo of the plate in Fig. 16(a), and the major elongation is given along the path in Fig. 16(b). The shape predicted here by the model using Mooney constitutive equations differs once again from the photograph. The local error also remains high for large strain (40% approximately). Consequently, even when the global

kinematics is imposed, the strain field is not well evaluated. Because of the strain heterogeneity, some areas of the specimen are very badly described, resulting in an inaccurate global prediction. The elongation in the most stretched part of the specimen is overestimated.

7. Conclusions

In order to make an experimental and numerical study of an unfilled silicone rubber, different aspects
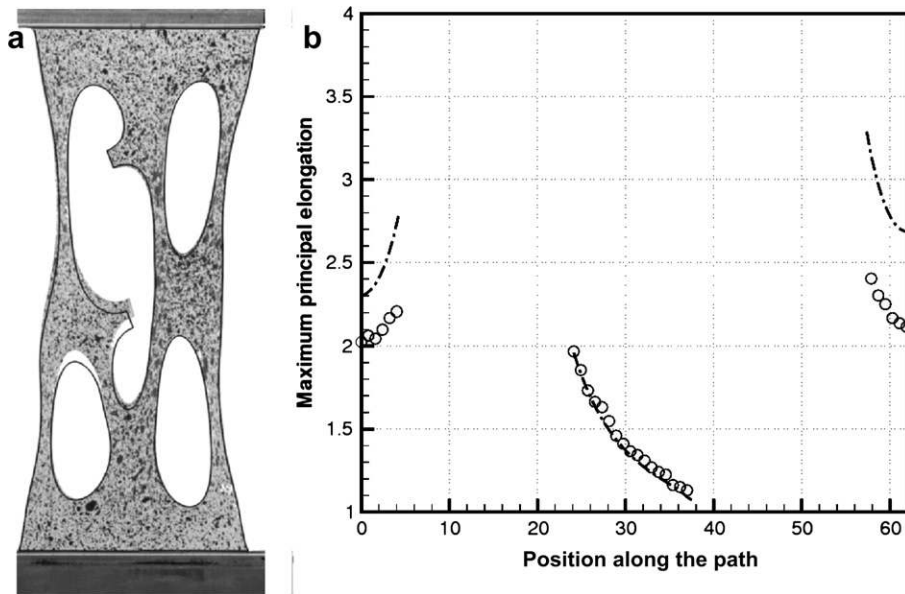

Fig. 16. Comparison of the experiment and Mooney model at an imposed displacement of 57.3 mm: (a) shapes, (b) major principal elongation along the path for experimental data (o) and Mooney (·–·).

have been addressed. First, the experimental procedures were detailed. Then several tests were developed to evaluate the mechanical behaviour of the silicone rubber. The results highlight the lack of Mullins effect, hysteresis and strain rate dependency, but different stress state could be measured for different homogeneous load cases (tensile, pure shear, compression, plane strain compression, bulge test). Thus, the considered silicone rubber has a non-linear elastic behaviour, i.e., its mechanical behaviour is entirely defined by its elastic energy. Hence, different hyperelastic constitutive equations were used to model its behaviour since these models express the energy density of the material. These models were fitted to the experimental data and evaluated. Finally, the chosen silicone rubber could be used as a model material to test the capability of models to predict material behaviour. This takes advantage of the uncommon characteristic of this silicone to be perfectly elastic in finite strain.

To develop further comparisons, a plate with holes was stretched while measuring the strain field. Finite element analysis using Gent, Haines and Wilson and Ogden constitutive equations provided results in good agreement with experimental data. However, caution is necessary because Haines and Wilson and Ogden need six parameters that are tricky to fit, especially if few experimental data are available. Gent is a little bit less accurate but makes coherent predictions for any load case. Contrary to the previous cited models, Mooney largely overestimated the strain levels in the most stretched parts of the plate. This conclusion was logical with regard to the capacity of this constitutive equation to represent the strain hardening. So, at an imposed load, the model's predictions were too large. However, to further investigate this model's predictions, the conditions of the numerical model were changed to impose displacement, but once again large overestimations of the elongation remained.

These results highlight the need to be very cautious when fitting hyperelastic constitutive equations and using them for numerical simulations. In particular, using the Mooney model to run analysis can lead to large overestimations in all very stressed parts, in particular in the case of crack tip analysis where the considered area is the most highly stretched.

Acknowledgement

References

[1] N. Goulbourne, E. Mockensturm, M. Precker, Electro-elastomers: large deformation analysis of silicone membranes, Int. J. Solids Struct. 44 (2007) 2609–2626.
[2] P. Meier, M. Lang, S. Oberthür, Reiterated tension testing of silicone elastomer, Plast., Rubber Compos. Process. Appl. 34 (2005) 372–377.
[3] R. Loew, P. Meier, Simulation of reiterated mechanical load of silicone rubber, Finite Elem. Anal. Des. 43 (2006) 453–462.
[4] L. Mullins, Softening of rubber by deformation, Rubber Chem. Technol. 42 (1969) 339–362.
[5] E. Podnos, E. Becker, J. Klawitter, P. Strzepa, FEA analysis of silicone MCP implant, J. Biomech. 39 (2006) 1217–1226.
[6] O. Shergold, N. Fleck, D. Radford, The uniaxial stress versus strain response of pig skin and silicone rubber at low and high strain rates, Int. J. Impact Eng. 32 (2006) 1384–1402.
[7] L.R.G. Treolar, The elasticity of a network of long chain molecules (I and II), Trans. Faraday Soc. 39 (1943) 36–64 241–246.
[8] M. Mooney, A theory of large elastic deformation, J. Appl. Phys. 11 (1940) 582–592.
[9] R. Ogden, Large deformation isotropic elasticity – on the correlation of theory and experiment for incompressible rubberlike solids, Proc. R. Soc. London A326 (1972) 565–584.
[10] D. Haines, D. Wilson, Strain energy density functions for rubber like materials, J. Mech. Phys. Solids 27 (1979) 345–360.
[11] A. Gent, A new constitutive relation for rubbers, Rubber Chem. Technol. 69 (1996) 59–61.
[12] P. Vacher, S. Dumoulin, F. Morestin, S. Mguil-Touchal, Bidimensional strain measurement using digital images, Instn Mech Engrs Part C ImechE 213 (1999) 811–817.
[13] D. Favier, H. Louche, P. Schlosser, L. Orgéas, P. Vacher, L. Debove, Homogeneous and heterogeneous deformation mechanisms in an austenitic polycrystalline Ti-50.8 at.% Ni thin tube under tension. Investigation via temperature and strain fields measurements, Acta Mater. 55 (2007) 5310–5322.
[14] M. Giton, A.-S. Caro-Bretelle, P. Ienny, Hyperelastic behaviour identification by forward problem resolution: application to a tear test of silicone-rubber, Strain 42 (2006) 291–297.
[15] P. Dumont, L. Orgéas, S. LeCorre, D. Favier, Anisotropic viscous behaviour of sheet molding compounds (smc) during compression molding, Int. J. Plast. 19 (2003) 625–646.
[16] R. Rivlin, D. Saunders, Large elastic deforamtions of isotropic materials, Philos. Trans. R. Soc. London, Ser. A A243 (1651) 251–288.
[17] E. Boyce, Direct comparison of the Gent and Arruda–Boyce constitutive models of rubber elasticity, Rubber Chem. Technol. 69 (1996) 781–785.
[18] E. Arruda, M. Boyce, A three dimensional constitutive model for large stretch behaviour of rubber elastic materials, J. Mech. Phys. Solids 41 (1993) 389–412.
[19] L. Hart-Smith, Elasticity parameters for finite deformations of rubber like materials, Z. Angew. Math. Phys. 17 (1966) 608–626.
[20] G. Chagnon, E. Verron, G. Marckmann, A comparison of the physical model of Arruda–Boyce with the empirical Hart–Smith model and the Gent model, Rubber Chem. Technol. 77 (2004) 724–735.
[21] P. Heuillet, L. Dugautier, Modélisation du comportement hyperélastique des élastomères compacts, in: Génie Mécanique des caoutchoucs et des élastomères thermoplastiques, Apollor Inpl LRCCP Firtech edition, 1997, pp. 67–103.